J Adv Ceram

Research Article

High energy storage performance in the $Bi_{0.5}Na_{0.5}TiO_3$–$BaTiO_3$–$Nd(Mg_{1/2}Hf_{1/2})O_3$ ternary system with multiscale polymorphic domains and local heterogeneous structure

Changbai Long[1,✉], Ziqian Su[1], Anwei Xu[1], Fenglong Li[1], Yang Li[2], Wei Ren[2], Haijun Wu[1,✉], Xiangdong Ding[1,✉], Laijun Liu[3,✉]

Cite this article: Long C, Su Z, Xu A, et al. *J Adv Ceram* 2025, **14**(4): 9221063. https://doi.org/10.26599/JAC.2025.9221063

ABSTRACT: Lead-free dielectric relaxor ferroelectric (RFE) ceramics are one of the promising materials for dielectric energy storage applications. However, the contradiction between high polarization and low hysteresis leads to interior energy storage performance, which greatly limits their applications in high/pulsed power systems. Here, we propose an effective strategy to significantly improve the energy storage properties of $0.94Bi_{0.5}Na_{0.5}TiO_3$–$0.06BaTiO_3$ (0.94BNT–0.06BT) with a morphotropic phase boundary (MPB) composition by constructing multiscale polymorphic domains and local heterogeneous structures. The introduction of $Nd(Mg_{1/2}Hf_{1/2})O_3$ (NMH) facilitates the formation of short-range ordered polar nanoregions (PNRs). Moreover, small amounts of nanodomains with high polarization are resulted from local heterogeneous structures with Bi- and Ti-rich regions. Multiscale polymorphic domains with the coexistence of rhombohedral/tetragonal (R+T) nanodomains and PNRs ensure both high polarization and low hysteresis, which is crucial for improving the energy storage performance. Furthermore, the excellent electrical insulation is resulted from the high insulation resistivity, grain size at the submicron scale and a wide band gap by NMH doping. Therefore, a high recoverable energy density (W_{rec}) of 7.82 J/cm³ with an ultrahigh efficiency (η) of 93.1% is realized in the designed BNT–BT–NMH ternary system because of both a large ΔP and high E_b. These findings, together with good temperature/frequency/cycling stability, indicate that the optimum composition ceramics are very promising materials for energy storage applications in high/pulsed power systems.

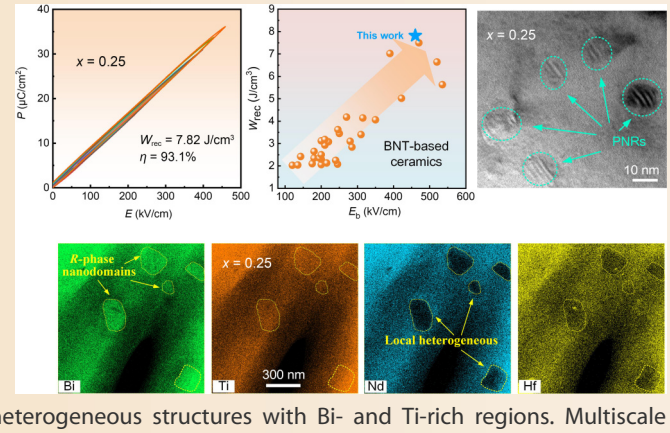

KEYWORDS: lead-free dielectric capacitors; $Bi_{0.5}Na_{0.5}TiO_3$ (BNT)-based ceramics; energy storage performance; multiscale polymorphic domains; local heterogeneous structure; dielectric breakdown electric strength

1 Introduction

Currently, the exploitation and use of renewable energy sources are the most urgent issues worldwide, with the increasing depletion of traditional energy sources such as oil and natural gas and the worsening of environmental pollution caused by them. Considering the intermittent nature of most renewable energy sources, it is required to develop various efficient and reliable energy storage technologies [1–3]. Dielectric capacitors have advantages over lithium batteries, fuel cells, and electrochemical capacitors in terms of high power density, fast charge/discharge rate, and high operating voltage, and thus they show great potential in applications such as hybrid vehicles, microwave communications, and pulse power weapons [4–6]. At present, polymer-based dielectric capacitors are widely used in industrial products owing to their high recoverable energy density (generally

[1] State Key Laboratory for Mechanical Behavior of Materials, Xi'an Jiaotong University, Xi'an 710049, China. [2] State Key Laboratory for Manufacturing Systems Engineering & Electronic Materials Research Laboratory, Key Laboratory of the Ministry of Education, Xi'an Jiaotong University, Xi'an 710049, China. [3] Key Laboratory of New Processing Technology for Nonferrous Metal & Materials, Ministry of Education/Guangxi Key Laboratory of Optical and Electronic Materials and Devices/Collaborative Innovation Center for Exploration of Nonferrous Metal Deposits and Efficient Utilization of Resources, Guilin University of Technology, Guilin 541004, China.

✉ Corresponding authors. E-mail: C. Long, longchangbai@126.com; H. Wu, wuhaijunnavy@xjtu.edu.cn; X. Ding, dingxd@mail.xjtu.edu.cn; L. Liu, ljliu2@163.com

Received: September 15, 2024; Revised: February 21, 2025; Accepted: March 15, 2025

W_{rec} > 10 J/cm^3) and giant dielectric breakdown electric strength (E_b > 1000 kV/cm) [7]. In contrast, dielectric ceramics have many advantages over dielectric polymers, including high dielectric constant, high efficiency (η), good thermal stability, and good mechanical properties [7–10]. In recent years, much work has focused on lead-free dielectric ceramics to explore advanced energy storage capacitors from the viewpoints of environmental protection and human health [10–12]. However, their energy storage density (generally W_{rec} < 5 J/cm^3) needs to be improved to meet the requirements of electronic components and devices for miniaturization and lightweight.

In general, the total energy-storage density (W_{tol}), W_{rec}, and η of dielectric materials can be calculated by using Eqs. (1)–(3) [13]:

$$W_{tol} = \int_0^{P_{max}} E dP \quad (1)$$

$$W_{rec} = \int_{P_r}^{P_{max}} E dP \quad (2)$$

$$\eta = W_{rec}/W_{tol} \times 100\% \quad (3)$$

where P_r and P_{max} are the maximum polarization and remnant polarization in a polarization–electric field (P–E) hysteresis loop, respectively. Notably, the combination of a large polarization difference ($\Delta P = P_{max} - P_r$) and a high electric field (E) favors high W_{rec} in lead-free dielectric ceramics. Among different types of dielectric ceramics, relaxor ferroelectric (RFE) ceramics are among the most promising materials for electric energy storage because they commonly exhibit slim P–E loops with very low P_r values [14–16]. It is believed that RFEs can be produced by adjusting long-range ferroelectric domains to short-range ordered polar regions via chemical doping [7]. By introducing $Bi(Mg_{0.5}Zr_{0.5})O_3$ into $BaTiO_3$ (BT), Yuan *et al.* [17] found that long-range ferroelectric domains were transformed into highly dynamic polar nanoregions (PNRs), and thus, the energy storage performance was enhanced (W_{rec} ≈ 2.9 J/cm^3, η ≈ 86.8%). A high W_{rec} of ~6.7 J/cm^3 along with a high η of ~92% was achieved in $Bi(Zn_{2/3}Ta_{1/3})O_3$-doped $K_{0.5}Na_{0.5}NbO_3$ (KNN) ceramics by driving a specific temperature region between the temperature of maximum dielectric constant (T_m) and the Burns temperature (T_B) to room temperature and inducing highly active weakly-coupled PNRs in this region [18]. Notably, PNRs are stable at high temperatures beyond T_m, guaranteeing good thermal stability in terms of energy storage performance [19]. Therefore, RFE ceramics are considered among the most promising materials for high-temperature energy storage applications.

In lead-free RFE systems such as $SrTiO_3$, BT, KNN, and $BiFeO_3$ (BF), $Bi_{0.5}Na_{0.5}TiO_3$ (BNT)-based ceramics have attracted increasing attention for exploring advanced/cutting-edge energy storage capacitors in recent years [20–37]. Like Pb^{2+} in Pb-based materials, Bi^{3+} in BNT possesses a lone pair electronic $6s^2$ configuration, which is strongly hybridized with O 2p orbitals, resulting in a large spontaneous polarization (P_s ≥ 40 μC/cm^2) [7,12,38–41]. Specifically, BNT ceramics are relaxors with a diffuse phase transition from rhombohedral (R) to tetragonal (T) symmetry between T_s (~200 °C) and T_m (~320 °C) [42,43]. Therefore, a strategy of lowering T_s to near room temperature is proposed to improve the relaxation and energy storage properties of BNT-based ceramics. For example, the introduction of $Sr_{0.7}La_{0.2}TiO_3$ into the BNT matrix results in a typical RFE at room temperature; thus, the optimized W_{rec} and η reach ~4.14 J/cm^3 and ~92.2%, respectively [44]. From a microscopic perspective, the energy storage properties of BNT-based ceramics essentially depend on their domain configuration and polarization response. Shi *et al.* [45] reported that long-range ferroelectric domains were disrupted to form short-range nanodomains by introducing $BaSnO_3$ to $0.9BNT–0.1Ba_{0.85}Ca_{0.15}Zr_{0.1}Ti_{0.9}O_3$, leading to a remarkable improvement in energy storage performance (W_{rec} ≈ 4.97 J/cm^3, η ≈ 84.4%). A recent study revealed that a high W_{rec} of ~7.3 J/cm^3 accompanied by a high η of ~93% was achieved in $BNT–Sr_{0.7}Bi_{0.2}TiO_3–La(Mg_{0.5}Ti_{0.5})O_3$ ternary ceramics under a moderate E of 390 kV/cm because of the formation of highly dynamic rhombohedral/tetragonal (R+T) nanodomains and PNRs [46]. As expected, multiscale polymorphic domains ensure both high polarization and low hysteresis in BNT-based and other RFE ceramics, which is favorable for achieving high W_{rec} and η.

Furthermore, high electric insulation is critical for realizing high W_{rec} in BNT-based ceramics. Many factors affect the E_b of ceramics, such as grain size, point defects, porosity, band gap, second phase (impurities), and sample thickness [7,9,13]. Typically, a decrease in grain size is beneficial for improving E_b, according to an inverse relationship between E_b and grain size, i.e., $E_b \propto (\text{gain size})^{-\alpha}$ [7]. Gao *et al.* [47] reported that the average grain size was reduced to the submicron scale (~0.6 μm) by introducing $Bi(Mg_{0.5}Sn_{0.5})O_3$ into a $(Na_{0.5}Bi_{0.5})_{0.65}Sr_{0.35}TiO_3$ matrix and thus a high W_{rec} of ~6.68 J/cm^3 was obtained at 405 kV/cm. Specifically, both the electrical resistivity (ρ) and E_b of BNT-based ceramics can be improved by suppressing the formation of point defects (mainly oxygen vacancies ($V_O^{\cdot\cdot}$)). Yan *et al.* [48] proposed an A-site defect engineering strategy to reduce the oxygen vacancy concentration and the oxygen ionic conductivity; as a result, the W_{rec} and E_b of $Bi_{0.58}Na_{0.42}TiO_3$–0.25ST-based ceramics were increased to 5.63 J/cm^3 and 535 kV/cm, respectively. In addition, a wider band gap is expected to lead to a higher intrinsic E_b for energy storage ceramics. Therefore, Kang *et al.* [49] reported that the E_b of $BNT–Sr_{0.7}Bi_{0.2}TiO_3$ ceramics increased from 160 to 410 kV/cm when HfO_2 (E_g ≈ 5.5 eV) was introduced; correspondingly, the W_{rec} of the system increased from 2.2 to 5.5 J/cm^3. Similarly, the energy storage properties of BNT-based ceramics can be improved by introducing oxides with a wide band gap (e.g., Ta_2O_5, SnO_2, and/or MgO (E_g ≈ 4–7.5 eV)) [50–52].

It has been reported that morphotropic phase boundaries (MPBs) with multiphase coexistence can be constructed at room temperature by introducing BT, ST, and BKT into the BNT matrix, facilitating the enhancement of both the dielectric and piezoelectric properties [53–55]. The $(1–x)$BNT–xBT (BNT–BT) system has a typical MPB structure with coexisting R- and T-phases when x = 0.05–0.1 [56]. However, BNT–BT ceramics with MPB compositions are unsuitable for electric energy storage, because they maintain large polarization hysteresis [57–59]. With considerable efforts to optimize energy storage properties, achieving a high W_{rec} of ≥ 7 J/cm^3 and η of ≥ 90% is still challenging for BNT–BT system ceramics. In this work, we propose a synergistic optimization strategy, namely, simultaneously constructing multiscale polymorphic domains and high electric insulation, to greatly improve the W_{rec} and η of 0.94BNT–0.06BT ceramics. The nanodomains in the NR state of 0.94BNT–0.06BT grow into macrodomains induced by the electric field, resulting in large P_{max} and P_r [7]. However, the introduction of $Nd(Mg_{1/2}Hf_{1/2})O_3$ (NMH) can facilitate the formation of highly dynamic PNRs, which is desirable for energy storage applications. Moreover, small amounts of nanodomains with high polarization are remained because a local heterogeneous structure with Bi- and Ti-rich regions is established. Multiscale

polymorphic domains with the coexistence of R+T nanodomains and PNRs ensure both high polarization and low hysteresis, which is crucial for improving the energy storage properties of 0.94BNT–0.06BT. Furthermore, high electrical insulation is resulted from NMH doping by reducing the grain size, increasing electric resistivity and enhancing band gap. Therefore, a high energy storage performance with $W_{rec} \approx 7.82$ J/cm^3 and $\eta \approx 93.1\%$ is realized in the optimum composition with $x = 0.25$ at 460 kV/cm because of the coexistence of large ΔP and high E_b. The influence of NMH doping on the energy storage properties of 0.96BNT–0.06BT ceramics was studied in detail, as shown in Fig. 1.

2 Experimental

Dielectric ceramics of $(1-x)$(0.94BNT–0.06BT)–xNMH (x = 0, 0.2, 0.25, 0.3) were prepared by traditional solid-state reaction. The raw materials, including Bi_2O_3 (99.9%), TiO_2 (99%), Na_2CO_3 (99.8%), $BaCO_3$ (99.8%), Nd_2O_3 (99.9%), MgO (99.99%), and HfO_2 (99.9%) (all from Sinopharm Chemical Reagent Co., Ltd., China), were weighted according to their corresponding chemical formulas. Subsequently, the oxides were mixed and ball milled in ethanol for 8 h. The mixtures were dried and then calcined at 850 °C for 4 h. The calcined powders were remilled in ethanol for 12 h, dried, ground, and isostatically cold-pressed into pellets ~12 mm in diameter and ~1 mm in thickness under a pressure of 200 MPa for 5 min. Finally, the pressed pellets were sintered at 1100–1150 °C for 2–3 h.

The phase structure and purity of the prepared ceramics were monitored by an X-ray diffractometer (XRD; Cu Kα, Bruker D8-ADVANCE, Germany) at room temperature. For Rietveld refinements, the data of the ceramic powders at the micron scale were collected in the 2θ range of 10°–100° with a step size of ~0.02°. The microstructure of the ceramics was characterized by a scanning electron microscope (SEM; SU8230, Hitachi, Japan). Raman spectra of the ceramics were collected by using a LabRAM HR800 instrument (Horiba Jobin Yvon, Lyon, France). The transmission electron microscopy (TEM), high-resolution transmission electron microscopy (HR-TEM), high angle annular dark field scanning transmission electron microscopy (HAADF-STEM), and selected area electron diffraction (SAED) images were obtained by using an electron microscope equipped with energy-dispersive X-ray spectroscopy (EDS) (JEM-F200(HR), JEOL, Japan). The domain configuration was characterized by using a piezoresponse force microscope (PFM; Dimension ICON, Bruker, Germany) (cantilever type: DDESP, Bruker, diomand-coated tip; amplitude: 4 V; frequency: 45 kHz). Temperature dependence of dielectric property was measured by using a precision LCR meter (4284A, Agilent, USA) at various frequencies (100, 1k, 10k, 100k, and 1M Hz). P–E hysteresis loops of the samples were measured by using Radiant Precision Premier II (USA) and Aix ACCT TF-3000 (Germany) ferroelectric analyzers. Impedance spectra of the samples were obtained from 0.1 to 1 × 10^6 Hz by using a Princeton P4000A electrochemistry system. The actual charging/discharging performance was evaluated by using a capacitor charge-discharge test system (PK-CPR1701, PolyK Technologies, USA). Ag electrodes were fabricated at 550 °C for 30 min for electrical property measurements.

3 Results and discussion

The x = 0–0.25 ceramics exhibit a perovskite structure without any appreciable secondary phases, as indicated by their XRD patterns (Fig. S1(a) in the Electronic Supplementary Material (ESM)). This indicates that Nd^{3+}, Mg^{2+}, and Hf^{4+} are successfully dissolved in the lattices of 0.94BNT–0.06BT to form a solid solution when $x \leq 0.25$. Nevertheless, an impurity phase ($Nd_2Hf_2O_7$) is detected in the x = 0.3 ceramics upon further increasing NMH doping. These results imply that the maximum x in $(1-x)$(0.94BNT–0.06BT)–xNMH within a solid solution limit is between 0.25 and 0.3. In addition, the addition of NMH seems to suppress the formation of R phase in 0.94BNT–0.06BT, as

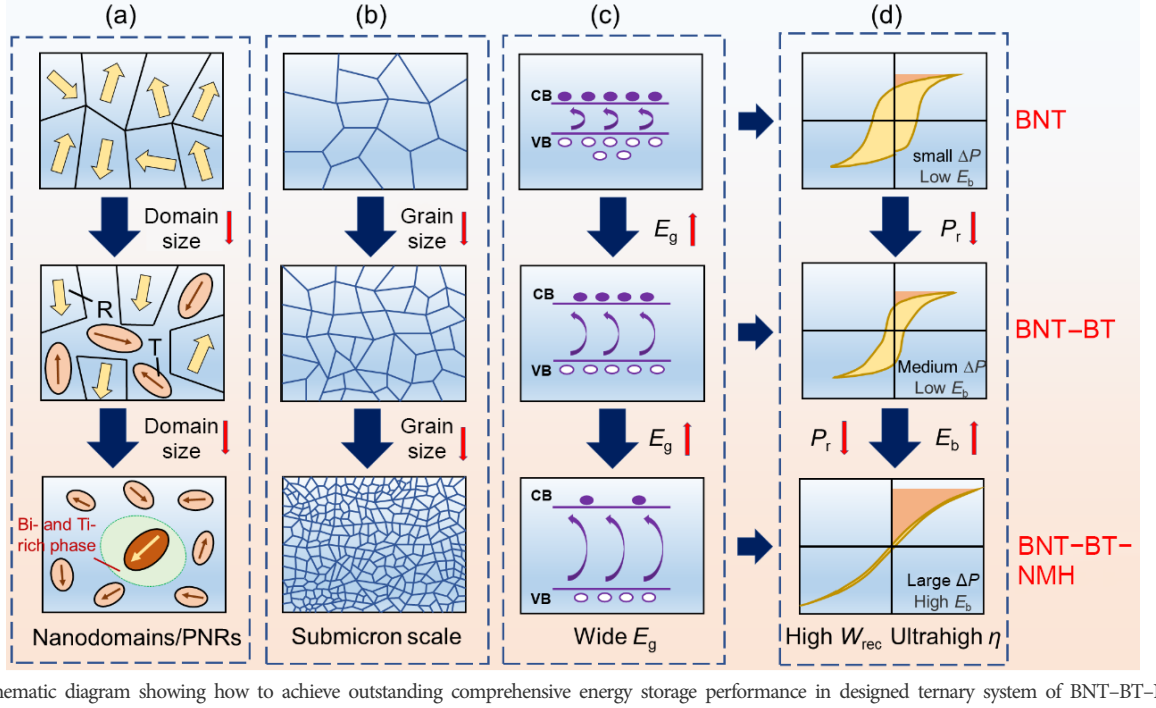

Fig. 1 Schematic diagram showing how to achieve outstanding comprehensive energy storage performance in designed ternary system of BNT–BT–NMH by constructing multiscale polymorphic domains, local heterogeneous structure, fine grains at the submicron scale, and excellent electric insulation with high E_g. "CB" and "VB" in (c) denote the conduction band and the valence band, respectively.

indicated by the disappearance of the shoulder peaks at $2\theta \approx 39.8°$ and 57.6° (Fig. S1(b) in the Electronic Supplementary Material (ESM)). Rietveld refinements of powder XRD data for $(1-x)$(0.94BNT–0.06BT)–xNMH reveal that the fraction of the R phase (space group: *R3c*) rapidly decreases from 46.1 to 9.8 wt% as x increases from zero to 0.3 (Fig. 2(e) in the ESM). Instead, the fraction of the T-phase (space group: *P4bm*) increases from 53.9 to 90.2 wt%. In general, the refined profile agrees well with the XRD pattern for each composition, as clearly shown in Figs. 2(a)–2(d). The final factors, R_{wp} and R_p, are stabilized to 6.62%–9.38% and 4.97%–5.71%, respectively; the values are greater for x = 0.3 than for x = 0–0.25 because of the appearance of impurity phase. According to the refined atomic parameters as listed in Table S1 in the ESM, the crystal structures of T and R phases for the composition with x = 0.25 are drawn in Fig. 2(f). Apparently, the structural distortion of R phase with strong polarization is more pronounced than that of T phase with weak polarization. In addition, both T and R phases show an increase in unit cell volume (V) with the addition of NMH, as shown in Figs. S2 and S3 in the ESM, respectively. This could be associated with the fact that the perovskite B site is occupied by larger cations and the dominant effect of BO_6 octahedra on V is more effective (Ti^{4+}: 0.605 Å, Mg^{2+}: 0.72 Å, Hf^{4+}: 0.71 Å; coordination number (CN): 6) [17,60].

To further explore the evolution of the local structure in the system, Raman spectra of all $(1-x)$(0.94BNT–0.06BT)–xNMH ceramics were measured in the wavenumber range from 50 to 1000 cm^{-1}. As shown in Fig. 2(g), four main regions are observed in the spectra, corresponding to A-site vibration (< 200 cm^{-1}), B–O vibration (200–400 cm^{-1}), the vibration of BO_6 octahedra (400–700 cm^{-1}), and A_1 and E overlapping bands (> 700 cm^{-1}), respectively [32,44]. Notably, all the Raman peaks gradually broaden with increasing NMH doping. After deconvolution by the Lorentz function, 8 Raman-active modes are detected in the spectra of the x = 0–0.3 ceramics. As shown in Fig. 2(h), the value of the full width at half maximum (FWHM) increases from 111 to 302 cm^{-1} for mode ν_1, from 142 to 182 cm^{-1} for mode ν_2 and from 120 to 138 cm^{-1} for mode ν_3, with increasing x in $(1-x)$(0.94BNT–0.06BT)–xNMH. These results indicate that the degree of structural distortion is lowered by introducing NMH. In contrast, the relaxation of the system is greatly improved because of the enhancement of both A-site and B-site disorders.

Figure 3(a) shows bipolar P–E loops of all $(1-x)$(0.94BNT–0.06BT)–xNMH ceramics recorded at 10 Hz. BNT–BT ceramics with MPB compositions are usually nonergodic relaxors (NRs) at room temperature, which tend to transform irreversibly into the ferroelectric phase under an electric field [7]. Therefore, the pure 0.94BNT–0.06BT ceramics exhibit saturation polarization with a high P_r of ~25.93 μC/cm² under a low electric field of 100 kV/cm, comparable to that of pure BNT ceramics [61]. The introduction of NMH likely results in a change from the NR state to the ergodic relaxor (ER) state by constructing highly dynamic PNRs (discussed later). Correspondingly, the square-like loop gradually evolves into a slim P–E loop, which is desirable for energy storage applications. In particular, the x = 0.25 and x = 0.3 ceramics show very slim loops with almost negligible P_r (~0.5 μC/cm²) and thereby high η values, as expected. Most importantly, good insulation is critical for realizing high W_{rec}. Here, the E_b of $(1-x)$(0.94BNT–0.06BT)–xNMH ceramics is evaluated by using the Weibull distribution law (Eqs. (4) and (5)) [62]:

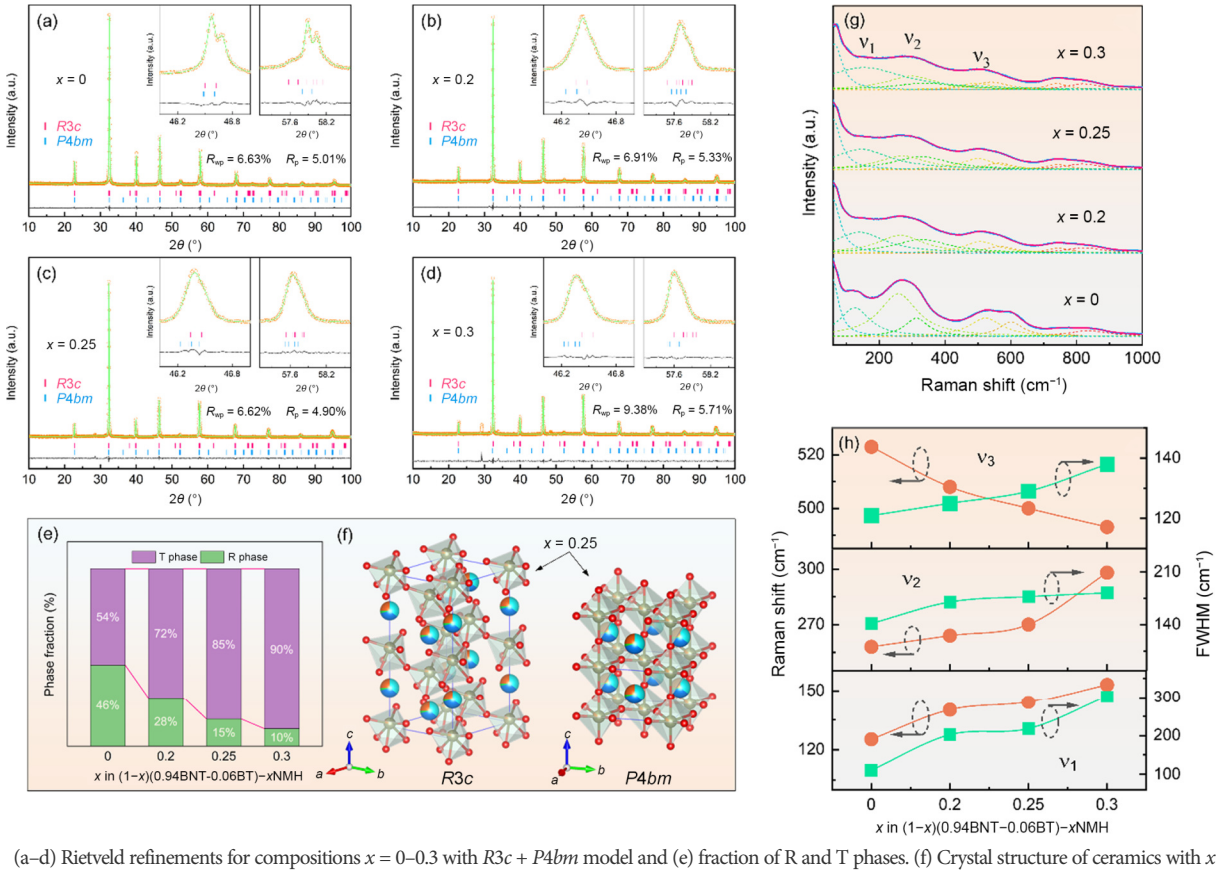

Fig. 2 (a–d) Rietveld refinements for compositions x = 0–0.3 with *R3c* + *P4bm* model and (e) fraction of R and T phases. (f) Crystal structure of ceramics with x = 0.25 composition. (g) Raman spectra of all $(1-x)$(0.94BNT–0.06BT)–xNMH ceramics at room temperature and (h) evolution of peak position and FWHM of modes ν_1, ν_2, and ν_3 with increasing x.

$$X_i = \ln(E_i) \tag{4}$$

$$Y_i = \ln\left(-\ln(1 - i/(n+1))\right) \tag{5}$$

where n is the total number of samples; i is the order number; E_i is the specific breakdown electric field of the i-th sample. The collected data points of all the compositions are in good agreement with the Weibull distribution accompanied by a large shape parameter ($\beta \approx 8.2$–12.6), as clearly shown in Fig. 3(b). Significantly, the E_b of the system is greatly improved by introducing NMH doping, and the maximum value is obtained for $x = 0.25$. The average E_b of the $x = 0.25$ ceramics is calculated to be ~459.9 kV/cm, approximately four times that of the $x = 0$ ceramics (~127.8 kV/cm). With further increasing NMH doping, the E_b of the $x = 0.3$ ceramics abnormally decreases to ~320.6 kV/cm, which should be associated with the existence of an impurity phase. In addition, the increase in grain size could lead to a decrease in E_b for $x = 0.3$ (see Fig. S6 in the ESM, as discussed later (next to Fig. 8)).

To evaluate the energy storage performance of the studied $(1-x)$(0.94BNT–0.06BT)–xNMH ceramics, their unipolar P–E loops were measured under electric fields near their E_b, as shown in Fig. 3(c). Subsequently, the W_{rec} and η values of all the compositions can be calculated by using Eqs. (1)–(3). Figure 3(d) shows that the pure 0.94BNT–0.06BT ceramics exhibit inferior energy storage properties associated with its large polarization hysteresis and low E_b ($W_{rec} \approx 1.05$ J/cm^3, $\eta \approx 65.6\%$). Importantly, both W_{rec} and η are significantly improved with the addition of NMH. Specifically, a high W_{rec} of 7.82 J/cm^3 with a high η of 93.1% is realized in the $x = 0.25$ ceramics because of the coexistence of a large ΔP (~35 μC/cm^2) and high E_b (~460 kV/cm). With further increasing NMH doping, the W_{rec} of the $x = 0.3$ ceramics rapidly decreases to 2.62 J/cm^3, which is evidently resulted from the decreased P_{max} and E_b. The P–E loops of the $x = 0.25$ ceramics under various electric fields are displayed in Fig. 3(e); correspondingly, W_{rec} and η as functions of electric field are given in Fig. 3(f). It is evident that the $x = 0.25$ ceramics always exhibit very slim P–E loops with nearly negligible P_r. Therefore, its η slightly decreases from 96.7% to 93.1% when the electric field is increased from 100 to 460 kV/cm. Notably, a sharp increase in W_{rec} is observed with increasing electric field, and the highest W_{rec} is obtained under the maximum electric field. As summarized in Fig. 3(g), the relationship between W_{rec} and E_b of the $x = 0.25$ ceramics and other BNT-based ceramics reveals that achieving a high E_b is one of the key factors for improving W_{rec}. Furthermore, comparisons of W_{rec} and η between the $x = 0.25$ ceramics and current lead-free dielectric ceramics are given in Fig. 3(h). The comprehensive energy storage performance of the $x = 0.25$ ceramics is superior to that of most existing RFEs and anti-ferroelectrics (AFEs), such as perovskite-structured (BT, BNT, $NaNbO_3$ (NN), KNN, BF, $AgNbO_3$ (AN), and $CaTiO_3$ (CT)) and tungsten bronze-structured (TTB) ceramics.

Importantly, the $x = 0.25$ ceramics show good temperature/frequency/cycling stability of the energy storage performance, which would provide them with an enormous range

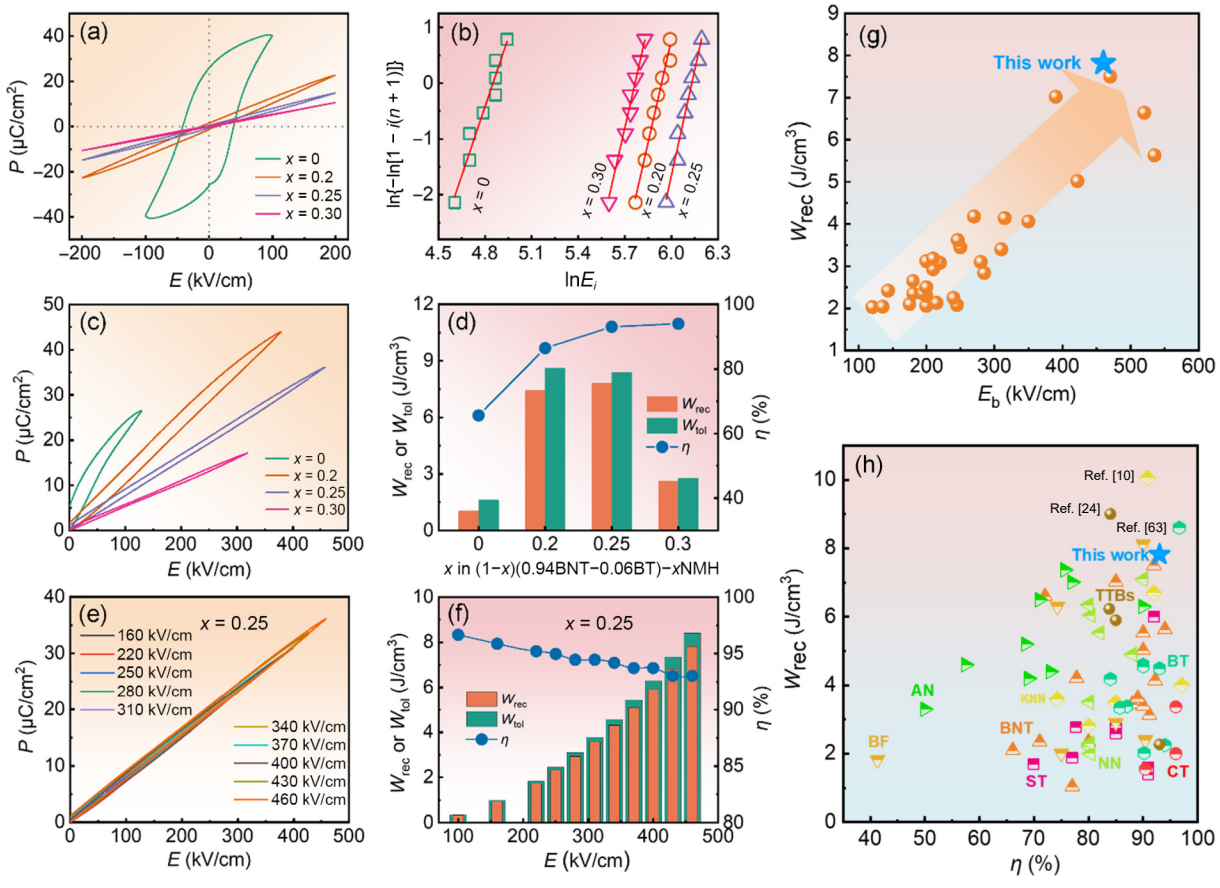

Fig. 3 (a) Bipolar P–E loops of all $(1-x)$(0.94BNT–0.06BT)–xNMH ceramics at room temperature and 10 Hz and (b) evaluation of E_b with Weibull distribution law. (c) Unipolar P–E loops of all $(1-x)$(0.94BNT–0.06BT)–xNMH ceramics and (d) their calculated W_{rec}, W_{tol}, and η under electric fields near their E_b. (e) Unipolar P–E loops of $x = 0.25$ ceramics under varied electric fields and (f) corresponding W_{rec}, W_{tol}, and η values. (g) Relationships between W_{rec} and E_b for $x = 0.25$ ceramics and other BNT-based ceramics reported in the literature. (h) Comparisons of W_{rec} and η between $x = 0.25$ ceramics and existing lead-free dielectric ceramics.

of application. As shown in Fig. 4(a), there is a small increase in both P_{max} and P_r for the $x = 0.25$ ceramics when the temperature is elevated from 20 to 160 °C. Consequently, it shows nearly stable W_{rec} with slight fluctuations in η under 300 kV/cm ($W_{rec} \approx 3.35\pm0.06$ J/cm^3, $\eta \approx 88.95\%\pm5.22\%$) (Fig. 4(b)). Good temperature stability ensures that the capacitors operate well over a wide temperature range, which is very important for their energy storage applications in many extreme environments [63]. Furthermore, the frequency stability and cyclic stability of energy storage ceramics should also be evaluated prior to their commercial applications. As presented in Fig. 4(c), the $x = 0.25$ ceramics always exhibit very slim P–E loops with nearly unchanged P_{max} under 350 kV/cm when the probing frequency is increased from 1 to 500 Hz. As a consequence, its energy storage properties are almost independent on the frequency ($W_{rec} \approx 4.33\pm0.09$ J/cm^3, $\eta \approx 93.96\%\pm2.85\%$) (Fig. 4(d)). Moreover, the shape and magnitude of the P–E loops under 350 kV/cm almost remain unchanged as the number of cycles increases from 1 to 1×10^5 (Fig. 4(e)). Therefore, it shows good cycling stability and W_{rec} and η are almost constant ($W_{rec} \approx 4.43\pm0.04$ J/cm^3, $\eta \approx 93.99\%\pm0.78\%$) (Fig. 4(f)). As presented above, good temperature/frequency/cycling stability provides an avenue for the $x = 0.25$ ceramics as good candidates for energy storage applications.

As mentioned above, the good temperature stability of the energy storage performance should be associated with the remarkable relaxor behavior. The temperature dependence of the dielectric constant (ε_r) and dielectric loss (tanδ) for all (1–x)(0.94BNT–0.06BT)–xNMH ceramics is shown in Figs. 5(a)–5(d). Two dielectric anomalies near T_s and T_m occur in the ε_r–T plot of the $x = 0$ ceramics, which should be resulted from the thermal evolution of *R3c* PNRs and the phase transition from *R3c* to *P4bm*, respectively [64,65]. Notably, the low-temperature anomaly near T_s gradually shifts towards room temperature when NMH is introduced to 0.96BNT–0.06BT. In particular, the T_s peaks not only become very diffuse but also exhibit a clear frequency dispersion with the addition of NMH. These results suggest that typical RFEs with remarkable relaxor behaviors are constructed in modified (1–x)(0.94BNT–0.06BT)–xNMH ceramics, which is highly desirable for their energy storage applications. The Vogel–Fulcher (V–F) model is employed to further investigate the evolution of PNRs (Eq. (6)) [66]:

$$f = f_0 \exp\left(\frac{E_a^*}{k_B(T_s - T_f)}\right) \quad (6)$$

where f_0 is a pre-exponential factor; E_a^* is the activation energy; T_f is the freezing temperature; k_B is the Boltzmann constant. The ln$f$ vs. T_s plots of the $x = 0.2$–0.3 ceramics are shown in Fig. 5(e). Their T_s values were estimated according to the dielectric maxima in the ε_r–T plots below 150 °C. The V–F fitting results reveal that their T_f decreases to temperatures far below room temperature (~185.1–218.8 K) (Fig. 5(f)). Therefore, modified ceramics should be the ER state material due to the high level of NMH doping. In addition, the E_a^* of the $x = 0.2$–0.3 ceramics is calculated to be ~0.25–0.32 eV, which is close to that of Bi($Zn_{2/3}Nb_{1/3}$)O_3-doped KNN ceramics (~0.22 eV) [67]. The activation energy denotes the energy barrier of the polarization fluctuation between adjacent polar clusters. Here, a high E_a^* with very low T_f suggests weak electrical coupling in modified compositions, facilitating the formation of highly dynamic PNRs.

Furthermore, *in situ* Raman spectra of the ceramics with optimum composition ($x = 0.25$) were measured to investigate the evolution of its local structure under varied temperature fields. Figure 5(g) shows that the variation in temperature has no obvious effect on the Raman spectra of the representative composition. The active Raman modes slightly shift towards lower wavenumbers with increasing temperature from –100 to 300 °C; for example, the peak position of mode ν_2 (A_1(TO)) decreases from ~269 to ~265 cm^{-1}, while that of mode ν_3 (E(TO)+A_1(LO)) decreases from ~503 to ~499 cm^{-1}. In particular, the spectral features of the $x = 0.25$ ceramics remain nearly unchanged between 0 and 200 °C, as clearly shown in Fig. 5(h). This is an indication that no local structural phase transition occurs over a wide temperature range. The stable phase structure is believed to be responsible for the good dielectric stability and energy storage stability of the $x = 0.25$ ceramics (Figs. 4(b) and 5(c)).

The variation in the domain structure is crucial for achieving high energy storage performance and strong relaxor behavior in

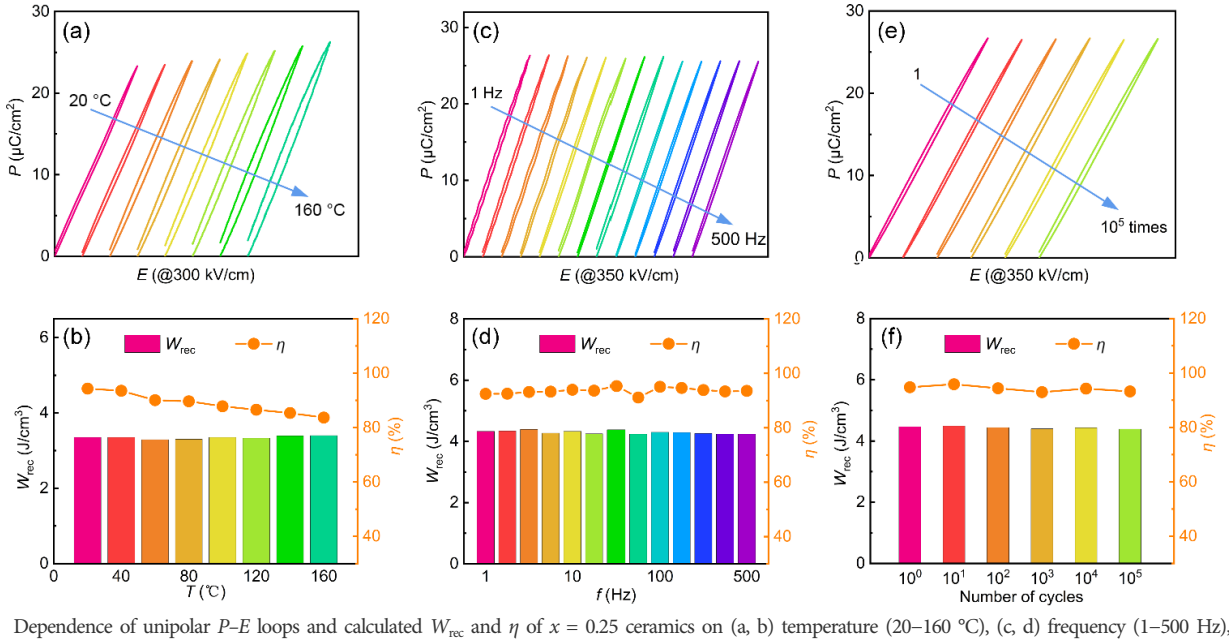

Fig. 4 Dependence of unipolar P–E loops and calculated W_{rec} and η of $x = 0.25$ ceramics on (a, b) temperature (20–160 °C), (c, d) frequency (1–500 Hz), and (e, f) number of cycles (1–1×10^5 times).

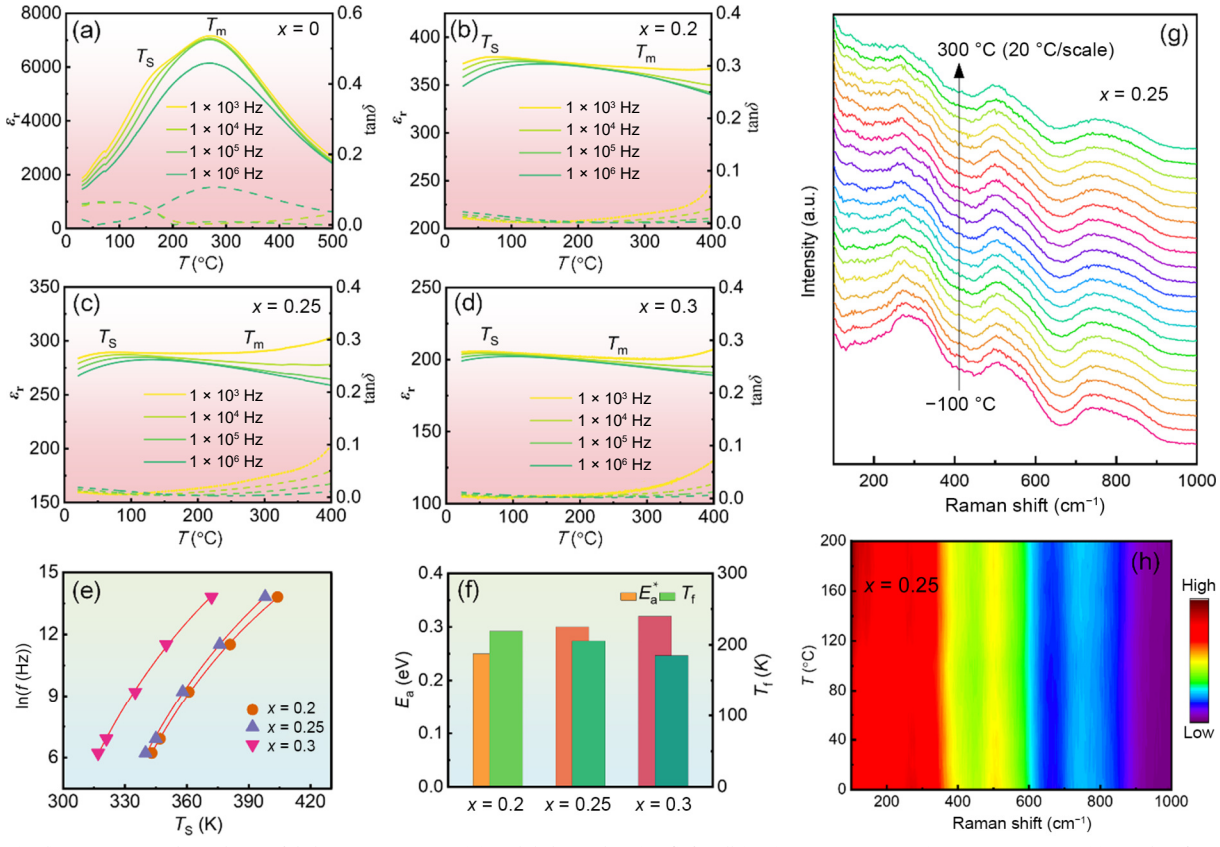

Fig. 5 (a–d) Temperature dependence of dielectric permittivity (ε_r) and dielectric loss (tanδ) for all (1−x)(0.94BNT–0.06BT)–xNMH ceramics. (e) Results of nonlinear V–F fitting for x = 0.2–0.3 ceramics and (f) extracted E_a^* and T_f values. (g) *In situ* Raman spectra of x = 0.25 ceramics over a wide temperature range from −100 to 300 °C and (h) evolution of spectral features between 0 and 200 °C.

the (1−x)(0.94BNT–0.06BT)–xNMH system. Here, TEM/HR-TEM analysis was performed to investigate the domain conformation and microstructure of the representative compositions with x = 0 and x = 0.25, as displayed in Figs. 6(a)–6(c). The pure 0.94BNT–0.06BT ceramics clearly have a complex domain structure composed of long-range ferroelectric domains that correspond to the presence of the rhombohedral *R*3c phase (Fig. 6(a)). It is likely that the long-range polarization order can be seriously broken by introducing high-concentration NMH to 0.94BNT–0.06BT. Therefore, no distinct domain structure can be observed in the x = 0.25 ceramics because the ordered polar regions are very small (Fig. 6(b)). Furthermore, the HR-TEM image of the x = 0.25 ceramics demonstrates that some nanosized regions present a feature of Moire fringes (Fig. 6(c)), originating from the interference of two overlaid lattice patterns with mismatched orientations [10,68]. The size of these mismatch regions is approximately 10 nm in radius, which is a typical scale for PNRs [68]. The formation of PNRs leads to low domain wall energy, which is beneficial for improving the relaxor behavior [69]. Accordingly, the x = 0.25 ceramics, as a typical RFE, demonstrate weak dielectric nonlinearity and very slim *P*–*E* loops with nearly negligible P_r, leading to the enhancement of energy storage performance.

Notably, the microstructure of the x = 0.25 ceramics shows nanoscale inhomogeneity in composition, as shown in Figs. 6(d)–6(k). The elemental analysis results reveal that Bi- and Ti-rich regions are involved in some grains because Nd^{3+}, Mg^{2+}, and Hf^{4+} are not sufficiently diffused into the perovskite structure. The low diffusion rates of foreign cations during sintering may explain the formation of a locally heterogeneous structure in the x = 0.25 ceramics. As shown in Figs. 6(l)–6(n), regions I and II with different chemical compositions exhibit similar SAED patterns recorded along the $[110]_c$ direction, indicating no obvious variation in the phase structure of the grains. As shown in region III in Fig. 6(d), weak 1/2{ooe} superlattice reflections are also observed in the $[001]_c$ SAED pattern of the x = 0.25 ceramics (Fig. 6(o)). The octahedral tilting of pure BNT results in superlattice reflections of type 1/2{ooo} for *R*3*c* and 1/2{ooe} for *P*4*bm* (o and e stand for the odd and even Miller indices, respectively) [13]. These results prove that the x = 0.25 ceramics have a multiphase structure with coexisting *R*3*c* and *P*4*bm* phases at room temperature. Compared with the other regions, the Bi- and Ti-rich regions in the x = 0.25 ceramics should have a higher fraction of R phase, as indicated by brighter 1/2{ooo} superlattice spots in region I than in region II (Figs. 6(m) and 6(n)). In contrast, the impurity phase $Nd_2Hf_2O_7$ mainly forms at the triangular grain boundaries of the x = 0.3 ceramics, as clearly shown in Fig. S4 in the ESM. TEM and HAADF-STEM images with EDS line scans also demonstrate that the Bi- and Ti-rich regions with sizes of ~100 nm remain in some grains of x = 0.3 ceramics (Figs. S4(g)–S4(i) in the ESM). The local heterogeneous structure with Bi- and Ti-rich regions is believed to favor the energy storage properties of (1−x)(0.94BNT–0.06BT)–xNMH ceramics.

PFM was further employed to provide insight into the domain structure and the dynamic response of the domains to the applied electric field in the (1−x)(0.94BNT–0.06BT)–xNMH ceramics. Figures 7(a) and 7(b) show out-of-plane phase and amplitude images of the x = 0 ceramics, respectively. It is clear that pure 0.94BNT–0.06BT demonstrates "strip-like" domain patterns with a strong amplitude response and a clear phase contrast, showing a long-range ferroelectric phase at room temperature [70]. NMH

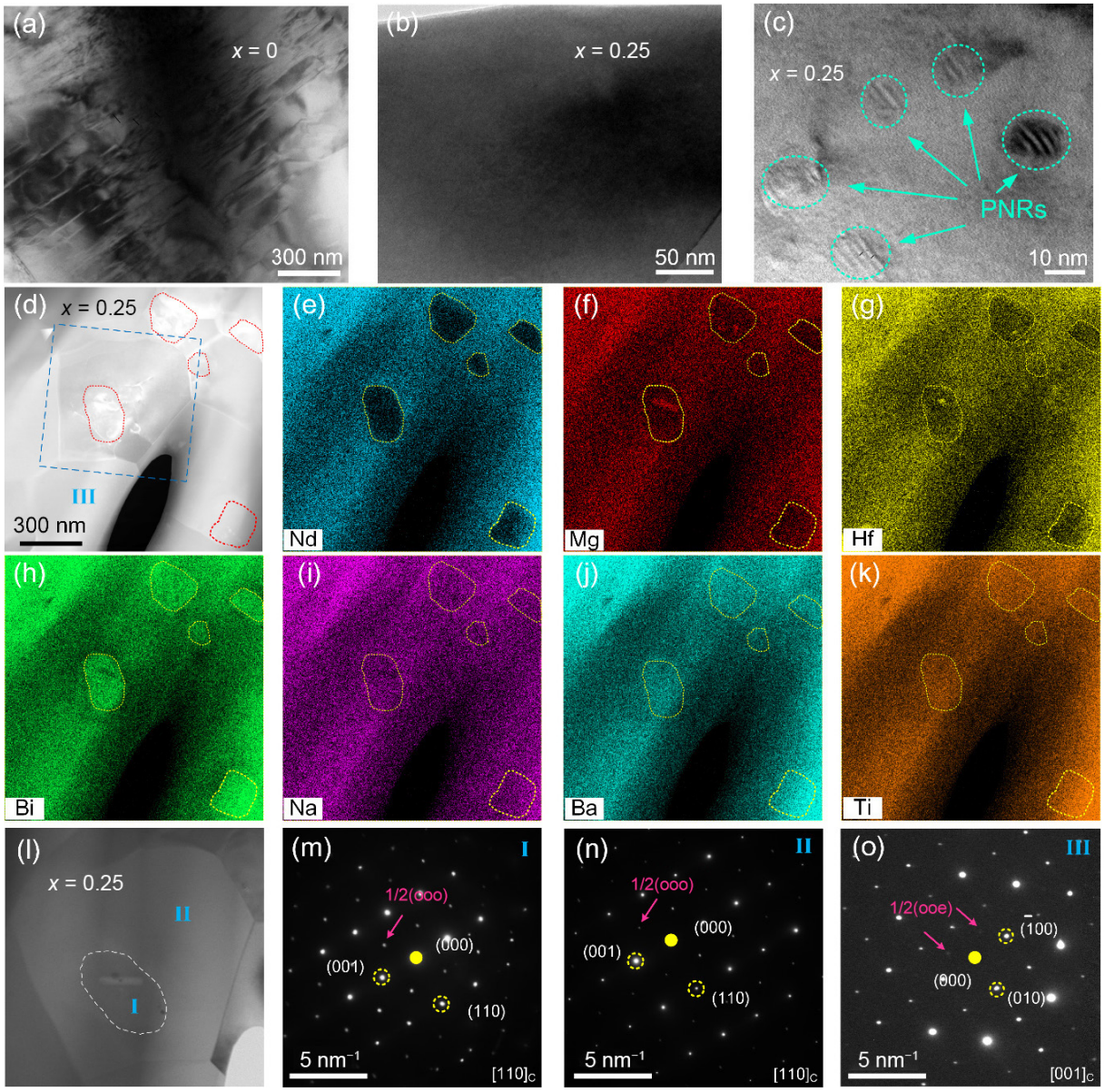

Fig. 6 (a, b) TEM and (c) HR-TEM images showing the domain structure of $x = 0$ and $x = 0.25$ ceramics. (d–k) HAADF-STEM and EDS mapping images revealing establishment of local heterogeneous structure in $x = 0.25$ ceramics. (l) TEM image of $x = 0.25$ ceramics viewed from the square frame shown in (d). (m, n) SAED patterns of $x = 0.25$ ceramics viewed from regions I and II shown in (l). (o) SAED pattern of $x = 0.25$ ceramics viewed from region III shown in (d).

doping leads to the establishment of short-range polarization order because of the enhancement of both A-site and B-site disorders. As a consequence, no clear domain structure is detected in the $x = 0.25$ ceramics at the limited resolution of PFM (Figs. 7(c) and 7(d)). Inspection of the figures reveals the existence of nanodomains, as seen in the center area of the blue square frame. As shown in Figs. 7(e) and 7(f), the size of nanodomains with a high piezoelectric response is approximately ~200 nm, which is close to that of the Bi- and Ti-rich regions (~150–300 nm, Figs. 6(g)–6(p)). The residual nanodomains with high polarization should be beneficial for achieving high P_{max} and W_{rec} in the $x = 0.25$ ceramics. PFM images of the $x = 0.25$ ceramics under both positive and negative direct current (dc) bias at an amplitude of 40 V are displayed in Figs. 7(g) and 7(h). Inspection of the phase image demonstrates that the polarization switching of the sample is incomplete because the switched domains quickly reverse back to the initial state. Specifically, all the domains can be rapidly recovered to the initial state in a short time of ~10 min after the external electric field is removed (Figs. 7(i)–7(l)). In contrast, the inner (−40 V) and outer (+40 V) square frames present distinct bright/dark contrasts of approximately 180°, reflecting that the electric field triggers reversible polarization switching (Figs. S5(a) and S5(b) in the ESM). In addition, the switched domains in the $x = 0$ ceramics are very stable, with a relaxation duration of ~10 min (Figs. S5(c)–S5(f) in the ESM). In summary, the experimental results above prove that highly dynamic PNRs are mainly formed in the $x = 0.25$ ceramics, which is conducive to its energy storage performance.

In addition to multiscale polymorphic domains, excellent electric insulation with high E_b is also an important factor in achieving high W_{rec} in the $x = 0.25$ ceramics. It has been reported that depletion space charge layers can be built at grain boundaries, which can act as barriers for the transport of charged carriers across grain boundaries [71]. Therefore, ceramics with small grain sizes commonly exhibit relatively high E_b values due to the high resistivity of grain boundaries. In the case of

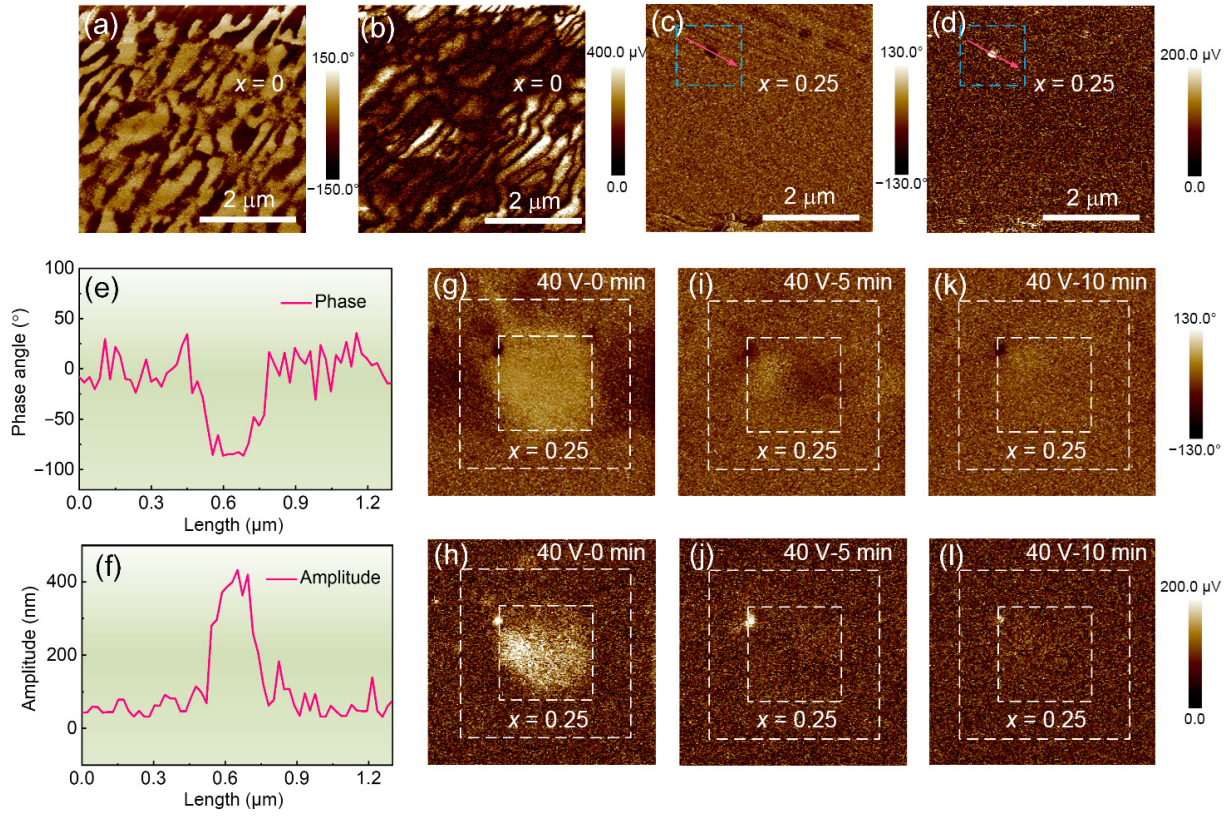

Fig. 7 (a–d) Out-of-plane PFM phase and amplitude images of $x = 0$ and $x = 0.25$ ceramics. (e, f) Variations in phase and amplitude at red lines in square frames shown in (c, d). (g–l) Domain writing of $x = 0.25$ ceramics at 40 V and (h–k) recovery of domains in short time of ~5 and ~10 min.

(1−x)(0.94BNT–0.06BT)–xNMH ceramics, the average grain size is obviously reduced by introducing NMH doping and is located at the minimum value (~0.63 μm) when $x = 0.25$ (Fig. S6 in the ESM). The substitution of nonvolatile Nd for volatile Bi and Na should effectively reduce the concentration of oxygen vacancies in the ceramics. The suppression of oxygen vacancies leads to a low diffusion rate in the grains and/or grain boundaries and thus slows grain growth [31]. Notably, the dense microstructure with a grain size at the submicron scale is helpful for enhancing the E_b of the $x = 0.25$ ceramics. Notably, the average grain size of the $x = 0.3$ ceramic slightly increased to ~0.76 μm with increasing NMH doping. This, together with the existence of an impurity phase, may lead to the fact that E_b is lower for $x = 0.3$ than for $x = 0.25$. The band gap (E_g) is the forbidden energy gap between the top of the valence band and the bottom of the conduction band, which can be calculated with the Tauc equation (Eq. (7)) [72]:

$$(\alpha h\nu)^2 = A\,(h\nu - E_g) \tag{7}$$

where $h\nu$, A, and α are the photon energy, a constant, and the absorption coefficient, respectively. Figure 8(a) displays the ultraviolet–visible (UV–Vis) absorbance spectra of all the (1−x)(0.94BNT–0.06BT)–xNMH ceramics. The E_g values can be derived from the extrapolation of the linear part of the corresponding $(\alpha h\nu)^2$ vs. $h\nu$ plots, as shown in Fig. 8(b). The addition of NMH results in an increase in E_g from 3.14 to 3.22 eV because of the incorporation of high-bandgap species (the E_g values of HfO_2 and MgO reach ~5.5 and ~7.7 eV, respectively). As expected, a wider band gap would lead to a higher intrinsic E_b for the $x = 0.2$–0.3 ceramics than for the $x = 0$ ceramics.

Notably, good electrical insulation in modified compositions should be closely related to the improvement in grain (bulk) resistivity (ρ_b). Here, the electrical conduction behaviors of all (1−x)(0.94BNT–0.06BT)–xNMH ceramics were evaluated by using electrochemical impedance spectroscopy (EIS). As indicated by the complex Z^* plots at 600 °C in Figs. 8(c)–8(f), the $x = 0$ ceramics exhibit a small semicircle at high frequencies and a large semicircle at low frequencies, corresponding to the grain effect and grain boundary effect, respectively. The same data presented in the Z''/M'' plots also show two component peaks associated with the grains and grain boundaries, as shown in Fig. 8(g). Notably, the size of semicircular grains increases with the addition of NMH. In particular, the complex Z^* plot of the $x = 0.3$ ceramics mainly consists of a large semicircle at high frequencies with a nearly negligible arc at low frequencies. Correspondingly, only the grain response is clearly identified by the Z''/M'' plots (Fig. 8(h)). These experimental results indicate that NMH doping leads to a significant increase in ρ_b. Arrhenius ρ_b plots of all the compositions over a wide temperature range from 300 to 600 °C are shown in Fig. 8(i). Inspection of the figure reveals that the ρ_b of $x = 0.2$–0.3 ceramics is approximately 1–4 orders of magnitude greater than that of the $x = 0$ ceramics. As a result, the total resistivity (ρ_{tol}) of the (1−x)(0.94BNT–0.06BT)–xNMH system is markedly increased by introducing NMH doping (Fig. 8(j)). Moreover, the addition of NMH leads to an increase in activity energy (E_a) for the conduction process; e.g., the E_a associated with the bulk resistivity is ~1.26–1.30 eV for $x = 0.2$–0.3, much higher than that for $x = 0$ (~0.31 eV). In summary, the high insulation resistivity combined with the grain size at the submicron scale and wide band gap ensures a high E_b in the $x = 0.25$ ceramics.

As mentioned above, a high energy storage performance with $W_{rec} \approx 7.82$ J/cm³ and $\eta \approx 93.1\%$ is realized in the designed (1−x)(0.94BNT–0.06BT)–xNMH system because of the coexistence of a large ΔP and high E_b. Importantly, the good temperature/frequency/cycling stability of the energy storage properties promote the actual applications of dielectric capacitors

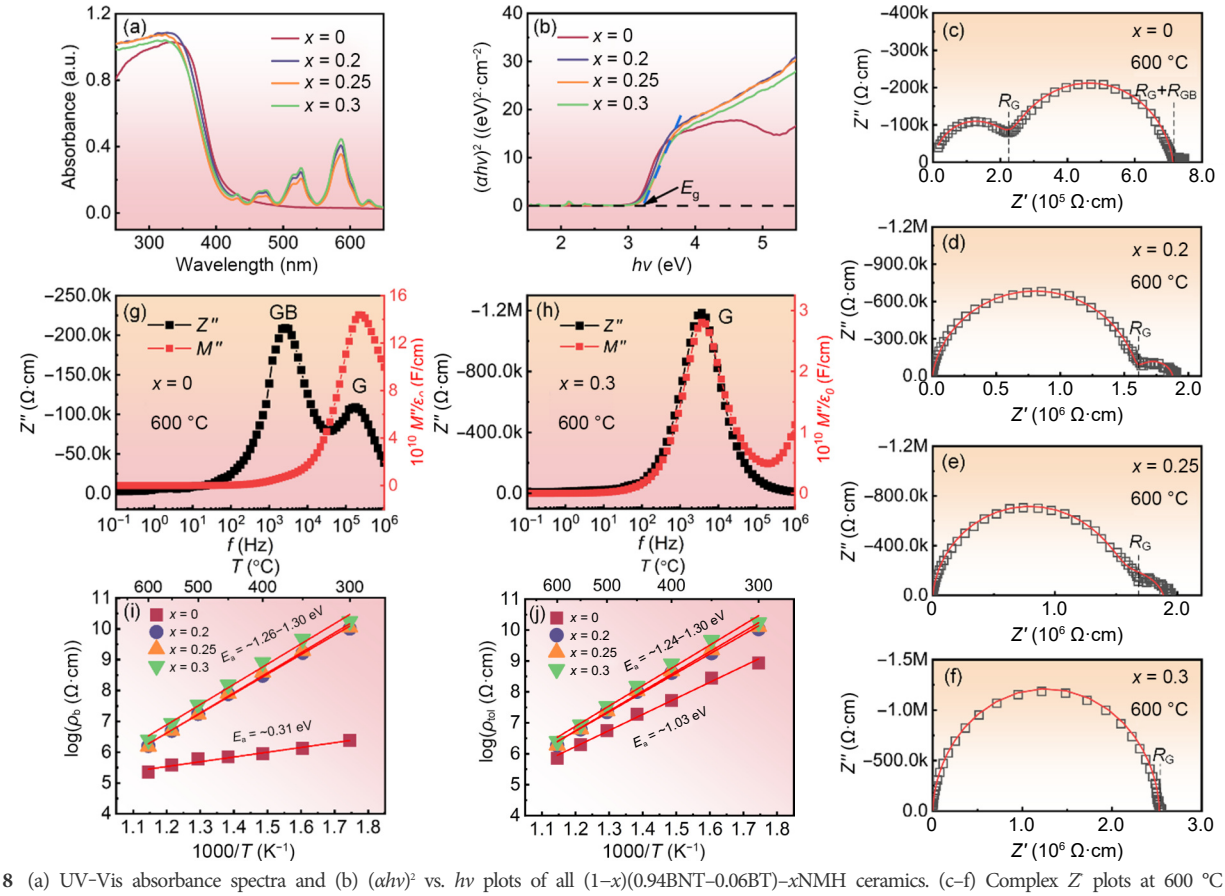

Fig. 8 (a) UV-Vis absorbance spectra and (b) $(\alpha h\nu)^2$ vs. $h\nu$ plots of all (1–x)(0.94BNT–0.06BT)–xNMH ceramics. (c–f) Complex Z plots at 600 °C for all (1–x)(0.94BNT–0.06BT)–xNMH ceramics and (g, h) the corresponding Z''/M'' plots for $x = 0$ and $x = 0.3$ ceramics. Arrhenius plots of logarithmic (i) ρ_b and (j) ρ_{tol} for all compositions over a temperature range from 300 to 600 °C.

over an enormous range of scales. Furthermore, the charge/discharge performance is critical for evaluating the potential for applications in high/pulsed power systems. Figure 9(a) shows the overdamped pulsed discharge current curves of the x = 0.25 ceramics under various electric fields. It is evident that the height of the current curves is gradually elevated as the electric field increases. The discharge energy density (W_D) can be calculated according to Eq. (8) [13]:

$$W_D = R\int i(t)^2 dt/V \quad (8)$$

where R, $i(t)$, and V are the load resistor (1 kΩ), discharge current, and sample volume, respectively. The W_D vs. t plots of the x = 0.25 ceramics under various electric fields are shown in Fig. 9(b). Inspection of the figure reveals that the plateau in the W_D vs. t plots is continuously raised by increasing the electric field from 40 to 320 kV/cm. Correspondingly, a monotonous increase in W_D is induced with increasing electric field (Fig. 9(g)). The highest W_D reaches 3.29 J/cm³ at 320 kV/cm, which is close to the calculated W_{rec} derived from the P–E loop under the same field. In addition, the discharge time ($t_{0.9}$), which is the time required to reach 90% of the maximum W_D, is nearly independent on the electric field [7]. Here, the x = 0.25 ceramics during the discharging process exhibit an extremely fast discharge rate with a low $t_{0.9}$ of ~0.44 μs. Importantly, the overdamped discharge current curves of the x = 0.25 ceramics nearly remain unchanged when the temperature is gradually elevated from room temperature (30 °C) to 170 °C, as clearly shown in Fig. 9(c). Correspondingly, the maximum W_D equivalent to the height of a distinct plateau in the W_D–t plots is almost independent on the temperature (W_D ≈ 2.07–2.19 J/cm³ under 250 kV/cm) (Figs. 9(d) and 9(g)). The underdamped charge–discharge performance as a function of the temperature and electric field is displayed in Figs. 9(e) and 9(f), respectively. Based on the underdamped pulsed discharge current curves, the corresponding current density ($C_D = I_{max}/S$, where I_{max} is the maximum current and S is the effective electrode area) and power density ($P_D = EI_{max}/2S$) can be calculated. Figure 9(h) shows that a monotonous increase in both C_D and P_D accompanies an increase in the electric field, and the highest values are obtained at 320 kV/cm (C_D ≈ 841.97 A/cm², P_D ≈ 134.71 MW/cm³). Nevertheless, both the C_D and P_D of the x = 0.25 ceramics at 250 kV/cm are nearly stable when the temperature is increased from room temperature (30 °C) to 170 °C (Fig. 9(i)). All of these results indicate that the x = 0.25 ceramics have good comprehensive charge–discharge performance; therefore, they can be treated as promising energy storage materials with great potential in high/pulsed power systems.

4 Conclusions

A novel ternary system of BNT–BT–NMH was designed to explore advanced dielectric energy storage capacitors. A remarkable enhancement in relaxor behavior is induced by introducing NMH to 0.94BNT–0.06BT ceramics with the MPB composition because of the enhancement of in A-site and B-site disorders. Significantly, highly dynamic PNRs are mainly formed in the studied (1–x)(0.94BNT–0.06BT)–xNMH ceramics, which is desirable for energy storage applications. Additionally, the residual nanodomains associated with the local heterogeneous structure are helpful for improving both P_{max} and W_{rec}. Multiscale

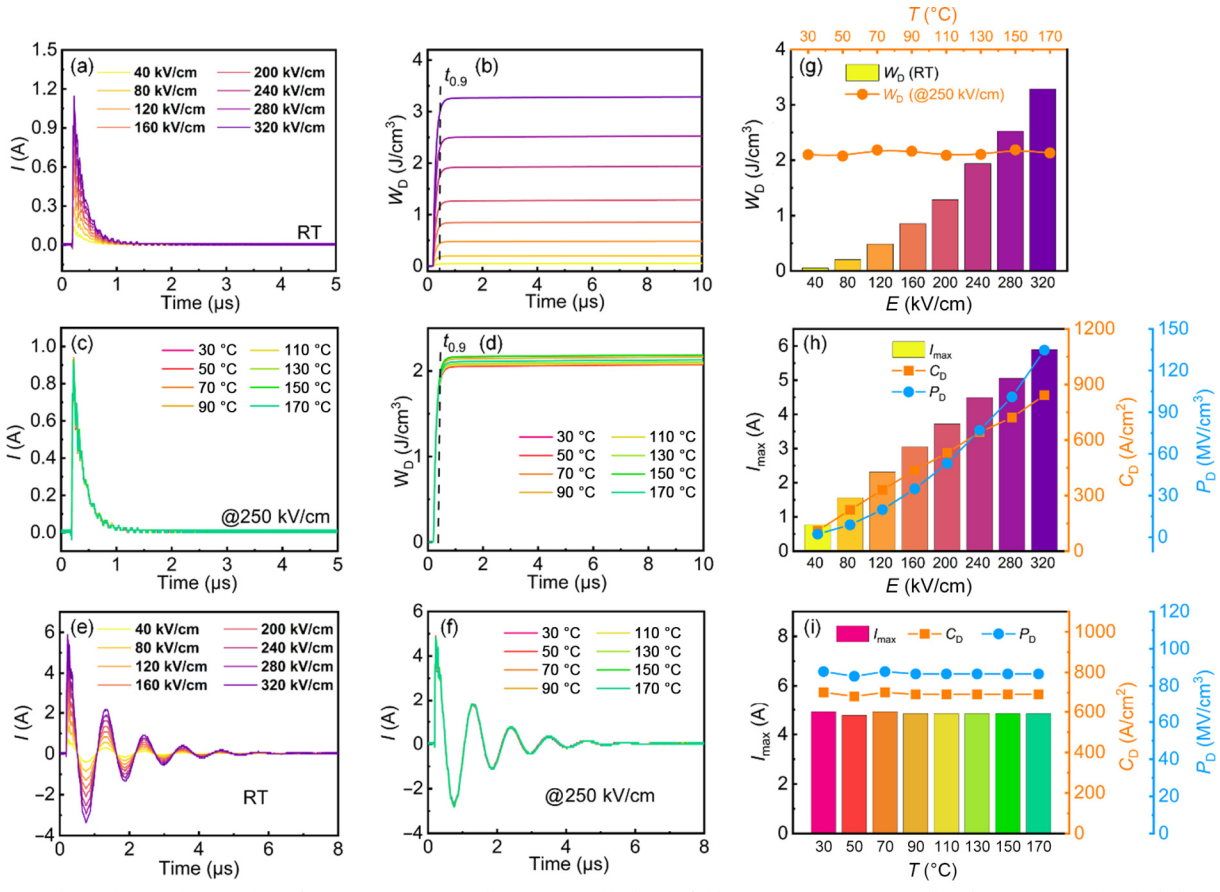

Fig. 9 Overdamped *I*–*t* and W_D–*t* plots of $x = 0.25$ ceramics under various (a, b) electric fields (room temperature) and (c, d) temperatures (applied electric field: 250 kV/cm). Underdamped *I*–*t* plots of $x = 0.25$ ceramics at various (e) electric fields (room temperature) and (f) temperatures (applied electric field: 250 kV/cm). (g) W_D and (h, i) I_{max}, C_D, and P_D as functions of electric field and temperature for $x = 0.25$ ceramics.

polymorphic domains with the coexistence of R+T nanodomains and PNRs ensure both high polarization and low hysteresis, which is critical to achieving high energy storage performance. In addition, excellent electrical insulation is mainly attributed to a significant increase in the bulk resistivity, a decrease in the grain size to the submicron scale, and a wider band gap. Therefore, high energy storage performance with $W_{rec} \approx 7.82$ J/cm³ and $\eta \approx 93.1\%$ is realized in the $x = 0.25$ ceramics because of both a large ΔP and high E_b. Furthermore, the $x = 0.25$ ceramics show good comprehensive charge–discharge performance, featuring a high C_D of ~841.97 A/cm² and P_D of ~134.71 MW/cm³, an acceptable W_D of ~3.29 J/cm³, and an ultrafast $t_{0.9}$ of ~0.44 μs at 320 kV/cm. These findings, together with good temperature/frequency/cycling stability, indicate that they are promising materials for energy storage applications in high/pulsed power systems.

Acknowledgments

This work was supported by the National Key R&D Program of China (No. 2021YFB3201100), the National Natural Science Foundation of China (Nos. 51931004, 12264012, 52172128 and 52472250), 111 Project 2.0 (No. BP2018008), the Natural Science Foundation of Guangxi (Nos. AB24010230, AA22068080, and AA23023027), and the Science and Technology Plan of Guilin (Nos. 2022H03 and ZY20220101).

Availability of data and materials

The data that support the findings of this study are available from the corresponding author upon reasonable request.

Competing interests

The authors have no competing interests to declare that are relevant to the content of this article.

Electronic Supplementary Material

Supplementary material is available in the online version of this article at https://doi.org/10.26599/JAC.2025.9221063.

References

[1] Guney MS, Tepe Y. Classification and assessment of energy storage systems. *Renew Sustain Energy Rev* 2017, **75**: 1187–1197.

[2] Panwar NL, Kaushik SC, Kothari S. Role of renewable energy sources in environmental protection: A review. *Renew Sustain Energy Rev* 2011, **15**: 1513–1524.

[3] Zhao PY, Cai ZM, Wu LW, *et al.* Perspectives and challenges for lead-free energy-storage multilayer ceramic capacitors. *J Adv Ceram* 2021, **10**: 1153–1193.

[4] Chu BJ, Zhou X, Ren KL, *et al.* A dielectric polymer with high electric energy density and fast discharge speed. *Science* 2006, **313**: 334–336.

[5] Li DX, Zeng XJ, Li ZP, *et al.* Progress and perspectives in dielectric energy storage ceramics. *J Adv Ceram* 2021, **10**: 675–703.

[6] Liu C, Li F, Ma LP, *et al.* Advanced materials for energy storage. *Adv Mater* 2010, **22**: E28–E62.

[7] Yang LT, Kong X, Li F, *et al.* Perovskite lead-free dielectrics for energy storage applications. *Prog Mater Sci* 2019, **102**: 72–108.

[8] Dou LY, Yang BB, Lan S, *et al.* Nanonet-/fiber-structured flexible ceramic membrane enabling dielectric energy storage. *J Adv Ceram* 2023, **12**: 145–154.

[9] Wang G, Lu ZL, Li Y, *et al.* Electroceramics for high-energy density capacitors: Current status and future perspectives. *Chem Rev* 2021, **121**: 6124–6172.
[10] Chen L, Deng SQ, Liu H, *et al.* Giant energy-storage density with ultrahigh efficiency in lead-free relaxors via high-entropy design. *Nat Commun* 2022, **13**: 3089.
[11] Luo NN, Han K, Cabral MJ, *et al.* Constructing phase boundary in $AgNbO_3$ antiferroelectrics: Pathway simultaneously achieving high energy density and efficiency. *Nat Commun* 2020, **11**: 4824.
[12] Qi H, Xie AW, Tian A, *et al.* Superior energy-storage capacitors with simultaneously giant energy density and efficiency using nanodomain engineered $BiFeO_3$–$BaTiO_3$–$NaNbO_3$ lead-free bulk ferroelectrics. *Adv Energy Mater* 2020, **10**: 1903338.
[13] Qi H, Xie AW, Zuo RZ. Local structure engineered lead-free ferroic dielectrics for superior energy-storage capacitors: A review. *Energy Storage Mater* 2022, **45**: 541–567.
[14] Sun Z, Zhang J, Luo HJ, *et al.* Superior capacitive energy-storage performance in Pb-free relaxors with a simple chemical composition. *J Am Chem Soc* 2023, **145**: 6194–6202.
[15] Hu QY, Tian Y, Zhu QS, *et al.* Achieve ultrahigh energy storage performance in $BaTiO_3$–$Bi(Mg_{1/2}Ti_{1/2})O_3$ relaxor ferroelectric ceramics via nano-scale polarization mismatch and reconstruction. *Nano Energy* 2020, **67**: 104264.
[16] Fan XH, Wang J, Yuan H, *et al.* Multi-scale synergic optimization strategy for dielectric energy storage ceramics. *J Adv Ceram* 2023, **12**: 649–680.
[17] Yuan QB, Li G, Yao FZ, *et al.* Simultaneously achieved temperature-insensitive high energy density and efficiency in domain engineered $BaTiO_3$–$Bi(Mg_{0.5}Zr_{0.5})O_3$ lead-free relaxor ferroelectrics. *Nano Energy* 2018, **52**: 203–210.
[18] Li D, Zhou D, Wang D, *et al.* Improved energy storage properties achieved in (K,Na)NbO_3-based relaxor ferroelectric ceramics via a combinatorial optimization strategy. *Adv Funct Mater* 2022, **32**: 2111776.
[19] Yang LT, Kong X, Cheng ZX, *et al.* Ultra-high energy storage performance with mitigated polarization saturation in lead-free relaxors. *J Mater Chem A* 2019, **7**: 8573–8580.
[20] Wu JY, Mahajan A, Riekehr L, *et al.* Perovskite $Sr_x(Bi_{1-x}Na_{0.97-x}Li_{0.03})_{0.5}TiO_3$ ceramics with polar nano regions for high power energy storage. *Nano Energy* 2018, **50**: 723–732.
[21] Guo J, Yu HF, Ren YF, *et al.* Multi-symmetry high-entropy relaxor ferroelectric with giant capacitive energy storage. *Nano Energy* 2023, **112**: 108458.
[22] Wang W, Zhang LY, Jing RY, *et al.* Enhancement of energy storage performance in lead-free barium titanate-based relaxor ferroelectrics through a synergistic two-step strategy design. *Chem Eng J* 2022, **434**: 134678.
[23] Liu S, Feng WW, Li JH, *et al.* Achieving high energy storage density and efficiency simultaneously in $Sr(Nb_{0.5}Al_{0.5})O_3$ modified $BiFeO_3$ based lead-free ceramics. *Chem Eng J* 2023, **451**: 138916.
[24] Gao YF, Qiao WJ, Lou XJ, *et al.* Ultrahigh energy storage in tungsten bronze dielectric ceramics through a weakly coupled relaxor design. *Adv Mater* 2024, **36**: 2310559.
[25] Zhu W, Shen ZY, Deng W, *et al.* A review: (Bi,Na)TiO_3 (BNT)-based energy storage ceramics. *J Materiomics* 2024, **10**: 86–123.
[26] Huang YL, Zhao CL, Wu B, *et al.* Multifunctional $BaTiO_3$-based relaxor ferroelectrics toward excellent energy storage performance and electrostrictive strain benefiting from crossover region. *ACS Appl Mater Inter* 2020, **12**: 23885–23895.
[27] Long CB, Su ZQ, Song HM, *et al.* Excellent energy storage properties with ultrahigh W_{rec} in lead-free relaxor ferroelectrics of ternary $Bi_{0.5}Na_{0.5}TiO_3$–$SrTiO_3$–$Bi_{0.5}Li_{0.5}TiO_3$ via multiple synergistic optimization. *Energy Storage Mater* 2024, **65**: 103055.
[28] Yang Q, Zhu MK, Wei QM, *et al.* Excellent energy storage performance of $K_{0.5}Bi_{0.5}TiO_3$-based ferroelectric ceramics under low electric field. *Chem Eng J* 2021, **414**: 128769.
[29] Dong XY, Li X, Chen HY, *et al.* Realizing enhanced energy storage and hardness performances in $0.90NaNbO_3$–$0.10Bi(Zn_{0.5}Sn_{0.5})O_3$ ceramics. *J Adv Ceram* 2022, **11**: 729–741.
[30] Lu ZL, Bao WC, Wang G, *et al.* Mechanism of enhanced energy storage density in $AgNbO_3$-based lead-free antiferroelectrics. *Nano Energy* 2021, **79**: 105423.
[31] Long CB, Zhou WJ, Song HM, *et al.* Simultaneously realizing ultrahigh energy storage density and efficiency in $BaTiO_3$-based dielectric ceramics by creating highly dynamic polar nanoregions and intrinsic conduction. *Acta Mater* 2023, **256**: 119135.
[32] Ding YQ, Li P, He JT, *et al.* Simultaneously achieving high energy-storage efficiency and density in bi-modified $SrTiO_3$-based relaxor ferroelectrics by ion selective engineering. *Compos Part B Eng* 2022, **230**: 109493.
[33] Yin J, Zhang YX, Lv X, *et al.* Ultrahigh energy-storage potential under low electric field in bismuth sodium titanate-based perovskite ferroelectrics. *J Mater Chem A* 2018, **6**: 9823–9832.
[34] Han K, Luo NN, Mao SF, *et al.* Ultrahigh energy-storage density in A-/B-site co-doped $AgNbO_3$ lead-free antiferroelectric ceramics: Insight into the origin of antiferroelectricity. *J Mater Chem A* 2019, **7**: 26293–26301.
[35] Yang ZT, Du HL, Jin L, *et al.* High-performance lead-free bulk ceramics for electrical energy storage applications: Design strategies and challenges. *J Mater Chem A* 2021, **9**: 18026–18085.
[36] Li DX, Shen ZY, Li ZP, *et al.* *P*–*E* hysteresis loop going slim in $Ba_{0.3}Sr_{0.7}TiO_3$-modified $Bi_{0.5}Na_{0.5}TiO_3$ ceramics for energy storage applications. *J Adv Ceram* 2020, **9**: 183–192.
[37] Li ZP, Li DX, Shen ZY, *et al.* Remarkably enhanced dielectric stability and energy storage properties in BNT–BST relaxor ceramics by A-site defect engineering for pulsed power applications. *J Adv Ceram* 2022, **11**: 283–294.
[38] Zhu CQ, Cai ZM, Luo BC, *et al.* High temperature lead-free BNT-based ceramics with stable energy storage and dielectric properties. *J Mater Chem A* 2020, **8**: 683–692.
[39] Wu YC, Fan YZ, Liu NT, *et al.* Enhanced energy storage properties in sodium bismuth titanate-based ceramics for dielectric capacitor applications. *J Mater Chem C* 2019, **7**: 6222–6230.
[40] Ji HF, Wang DW, Bao WC, *et al.* Ultrahigh energy density in short-range tilted NBT-based lead-free multilayer ceramic capacitors by nanodomain percolation. *Energy Storage Mater* 2021, **38**: 113–120.
[41] Feng Q, Liu X, Yuan CL, *et al.* Enhanced energy storage properties of $Bi_{0.5}Li_{0.5}TiO_3$ modified $Sr_{0.1}Bi_{0.45}Na_{0.45}TiO_3$ based ceramics. *J Adv Ceram* 2016, **5**: 219–224.
[42] Schmitt LA, Hinterstein M, Kleebe HJ, *et al.* Comparative study of two lead-free piezoceramics using diffraction techniques. *J Appl Crystallogr* 2010, **43**: 805–810.
[43] Jones GO, Thomas PA. Investigation of the structure and phase transitions in the novel A-site substituted distorted perovskite compound $Na_{0.5}Bi_{0.5}TiO_3$. *Acta Crystallogr B* 2002, **58**: 168–178.
[44] Qiao XS, Zhang FD, Wu D, *et al.* Superior comprehensive energy storage properties in $Bi_{0.5}Na_{0.5}TiO_3$-based relaxor ferroelectric ceramics. *Chem Eng J* 2020, **388**: 124158.
[45] Shi P, Zhu XP, Lou XJ, *et al.* Tailoring ferroelectric polarization and relaxation of BNT-based lead-free relaxors for superior energy storage properties. *Chem Eng J* 2022, **428**: 132612.
[46] Kang RR, Wang ZP, Wu M, *et al.* Superior energy storage capacity of a $Bi_{0.5}Na_{0.5}TiO_3$-based dielectric capacitor under moderate electric field by constructing multiscale polymorphic domains. *Nano Energy* 2023, **112**: 108477.
[47] Gao YF, Zhu XP, Yang B, *et al.* Grain size modulated $(Na_{0.5}Bi_{0.5})_{0.65}Sr_{0.35}TiO_3$-based ceramics with enhanced energy storage properties. *Chem Eng J* 2022, **433**: 133584.
[48] Yan F, Huang KW, Jiang T, *et al.* Significantly enhanced energy storage density and efficiency of BNT-based perovskite ceramics via A-site defect engineering. *Energy Storage Mater* 2020, **30**: 392–400.
[49] Kang RR, Wang ZP, Yang WJ, *et al.* Enhanced energy storage

performance of $Bi_{0.5}Na_{0.5}TiO_3$-based ceramics via grain tuning and relaxor construction. *Chem Eng J* 2023, **455**: 140924.

[50] Li X, Dong XY, Wang F, *et al.* Realizing excellent energy storage properties in $Na_{0.5}Bi_{0.5}TiO_3$-based lead-free relaxor ferroelectrics. *J Eur Ceram Soc* 2022, **42**: 2221–2229.

[51] Pu YP, Zhang L, Cui YF, *et al.* High energy storage density and optical transparency of microwave sintered homogeneous $(Na_{0.5}Bi_{0.5})_{(1-x)}Ba_xTi_{(1-y)}Sn_yO_3$ ceramics. *ACS Sustain Chem Eng* 2018, **6**: 6102–6109.

[52] Zhou XF, Qi H, Yan ZN, *et al.* Superior thermal stability of high energy density and power density in domain-engineered $Bi_{0.5}Na_{0.5}TiO_3$–$NaTaO_3$ relaxor ferroelectrics. *ACS Appl Mater Inter* 2019, **11**: 43107–43115.

[53] Sung YS, Kim JM, Cho JH, *et al.* Roles of lattice distortion in $(1-x)(Bi_{0.5}Na_{0.5})TiO_3$–$xBaTiO_3$ ceramics. *Appl Phys Lett* 2010, **96**: 202901.

[54] Hu D, Pan ZB, Zhang X, *et al.* Greatly enhanced discharge energy density and efficiency of novel relaxation ferroelectric BNT–BKT-based ceramics. *J Mater Chem C* 2020, **8**: 591–601.

[55] Sayyed S, Acharya SA, Kautkar P, *et al.* Structural and dielectric anomalies near the MPB region of $Na_{0.5}Bi_{0.5}TiO_3$–$SrTiO_3$ solid solution. *RSC Adv* 2015, **5**: 50644–50654.

[56] Kang WS, Koh JH. $(1-x)Bi_{0.5}Na_{0.5}TiO_3$–$xBaTiO_3$ lead-free piezoelectric ceramics for energy-harvesting applications. *J Eur Ceram Soc* 2015, **35**: 2057–2064.

[57] Li F, Yang K, Liu X, *et al.* Temperature induced high charge–discharge performances in lead-free $Bi_{0.5}Na_{0.5}TiO_3$-based ergodic relaxor ferroelectric ceramics. *Scripta Mater* 2017, **141**: 15–19.

[58] Ji XL, Li F, Long MS, *et al.* Excellent temperature stability of energy storage performance by weak dipolar interaction strategy. *Appl Phys Lett* 2022, **121**: 023902.

[59] Dong XY, Li X, Chen XL, *et al.* $(1-x)[0.90NN–0.10Bi(Mg_{2/3}Nb_{1/3})O_3]$ $–x(Bi_{0.5}Na_{0.5})_{0.7}Sr_{0.3}TiO_3$ ceramics with core–shell structures: A pathway for simultaneously achieving high polarization and breakdown strength. *Nano Energy* 2022, **101**: 107577.

[60] Shannon RD. Revised effective ionic radii and systematic studies of interatomic distances in halides and chalcogenides. *Acta Crystallogr A* 1976, **32**: 751–767.

[61] Long CB, Su ZQ, Xu AW, *et al.* $Bi_{0.5}Na_{0.5}TiO_3$-based energy storage ceramics with excellent comprehensive performance by constructing dynamic nanoscale domains and high intrinsic breakdown strength. *Nano Energy* 2024, **124**: 109493.

[62] Long CB, zhou WJ, Liu LJ, *et al.* Achieving excellent energy storage performances and eminent charging-discharging capability in donor $(1-x)$BT–x(BZN–Nb) relaxor ferroelectric ceramics. *Chem Eng J* 2023, **459**: 141490.

[63] Chen L, Hu TF, Shi XM, *et al.* Near-zero energy consumption capacitors by controlling inhomogeneous polarization configuration. *Adv Mater* 2024, **36**: 2313285.

[64] Wang ZP, Kang RR, Liu WY, *et al.* $(Bi_{0.5}Na_{0.5})TiO_3$-based relaxor ferroelectrics with medium permittivity featuring enhanced energy-storage density and excellent thermal stability. *Chem Eng J* 2022, **427**: 131989.

[65] He XF, Zhou S, Yuan Z, *et al.* The origin of weak coupling between polar clusters in Ta_2O_5-doped $0.94Bi_{0.5}Na_{0.5}TiO_3$–$0.06BaTiO_3$. *EPL Europhys Lett* 2020, **129**: 37004.

[66] Tagantsev AK. Vogel–Fulcher relationship for the dielectric permittivity of relaxor ferroelectrics. *Phys Rev Lett* 1994, **72**: 1100–1103.

[67] Huan Y, Wei T, Wang XZ, *et al.* Achieving ultrahigh energy storage efficiency in local-composition gradient-structured ferroelectric ceramics. *Chem Eng J* 2021, **425**: 129506.

[68] Liu Q, Zhang YC, Gao J, *et al.* High-performance lead-free piezoelectrics with local structural heterogeneity. *Energy Environ Sci* 2018, **11**: 3531–3539.

[69] Tao H, Wu HJ, Liu Y, *et al.* Ultrahigh performance in lead-free piezoceramics utilizing a relaxor slush polar state with multiphase coexistence. *J Am Chem Soc* 2019, **141**: 13987–13994.

[70] Wang Z, Zhao JY, Zhang N, *et al.* Optimizing strain response in lead-free $(Bi_{0.5}Na_{0.5})TiO_3$–$BaTiO_3$–$NaNbO_3$ solid solutions via ferroelectric/(non-) ergodic relaxor phase boundary engineering. *J Materiomics* 2023, **9**: 244–255.

[71] Waser R. TrI4: The role of grain boundaries in conduction and breakdown of perovskite-type titanates. *Ferroelectrics* 1992, **133**: 109–114.

[72] Li X, Cheng Y, Wang F, *et al.* Enhancement of energy storage and hardness of $(Na_{0.5}Bi_{0.5})_{0.7}Sr_{0.3}TiO_3$-based relaxor ferroelectrics via introducing $Ba(Mg_{1/3}Nb_{2/3})O_3$. *Chem Eng J* 2022, **431**: 133441.